

Deep learning reveals key predictors of thermal conductivity in covalent organic frameworks

Prakash Thakolkaran^{1,†} Yiwen Zheng^{2,†} Yaqi Guo¹ Aniruddh Vashisth^{2,*} Siddhant Kumar^{1,*}

¹Department of Materials Science and Engineering, Delft University of Technology, 2628 CD Delft, The Netherlands

²Department of Mechanical Engineering, University of Washington, Seattle, WA, USA

[†]Equal contribution

*Email: vashisth@uw.edu, sid.kumar@tudelft.nl; equal contribution

Keywords: *Covalent Organic Frameworks, Thermal Conductivity, Deep Learning, Attention*

The thermal conductivity of covalent organic frameworks (COFs), an emerging class of nanoporous polymeric materials, is crucial for many applications, yet the link between their structure and thermal properties remains poorly understood. Analysis of a dataset containing over 2,400 COFs reveals that conventional features such as density, pore size, void fraction, and surface area do not reliably predict thermal conductivity. To address this, an attention-based machine learning model was trained, accurately predicting thermal conductivities even for structures outside the training set. The attention mechanism was then utilized to investigate the model's success. The analysis identified dangling molecular branches as a key predictor of thermal conductivity, a discovery supported by feature importance assessments conducted on regression models. These findings indicate that COFs with dangling functional groups exhibit lower thermal transfer capabilities. Molecular dynamics simulations support this observation, revealing significant mismatches in the vibrational density of states due to the presence of dangling branches.

Introduction

Covalent organic frameworks [1, 2] (COFs) are an emerging class of nanoporous polymeric materials. Compared to metal-organic framework (MOFs) [3, 4] and zeolites [5], the crystalline backbone of COFs is composed of organic building blocks – known as knots and linkers – connected by strong covalent bonds, thereby offering higher stability [6]. The crystalline nature of COFs, along with their high surface areas, tunable pore sizes, and functionalizable organic linkers, make them exceptionally suited for a wide range of promising applications. These applications include (but are not limited to) photoconductivity [7, 8], chemo-sensing [9, 10], catalysis [11], drug delivery [12, 13], thermoelectrics [14, 15], semiconductors [16], gas storage and separation [17, 18].

A key property dictating the applications of COFs is thermal transfer. For example, low thermal conductivity is desired for thermoelectrics to maintain large internal thermal gradients and increase efficiency [19]. On the other hand, a high thermal conductivity is desired for gas adsorption and separation where efficient thermal transfer is important for the longevity and stability of the nanoporous membranes [20]. COFs are promising nanoporous candidates for such applications as the ability to design their crystalline topology (e.g., lattice type, pore size) and chemistry via choice of knots and linkers opens up a large and diverse space of thermal conductivities [21, 22, 23, 1, 2]. Therefore, it is of great interest to gain a deeper understanding of the thermal transfer mechanism and to obtain strong structure-property trends, which in turn enables the application-specific design of COFs.

Two approaches can be used to elucidate the thermal structure-property relationships of COFs: experimental trial-and-error methods which involve synthesis and characterization [24, 25], and computational high-throughput screening which relies on first-principle calculations [26, 27, 28]. With COFs offering practically an unlimited design space, an experimental trial-and-error approach to screen new COF candidates (including developing new synthesis routes for each candidate) is prohibitively inefficient. Moreover, experimentally synthesized COFs will always contain crystalline defects [29, 30], which greatly influence the thermal conductivity. This makes it difficult to relate the thermal transfer mechanisms to the geometrical and chemical make-up of a COF structure. On the contrary, molecular dynamics (MD) simulations [31] offer a high-throughput virtual screening alternative to lab-based experiments. However, despite recent

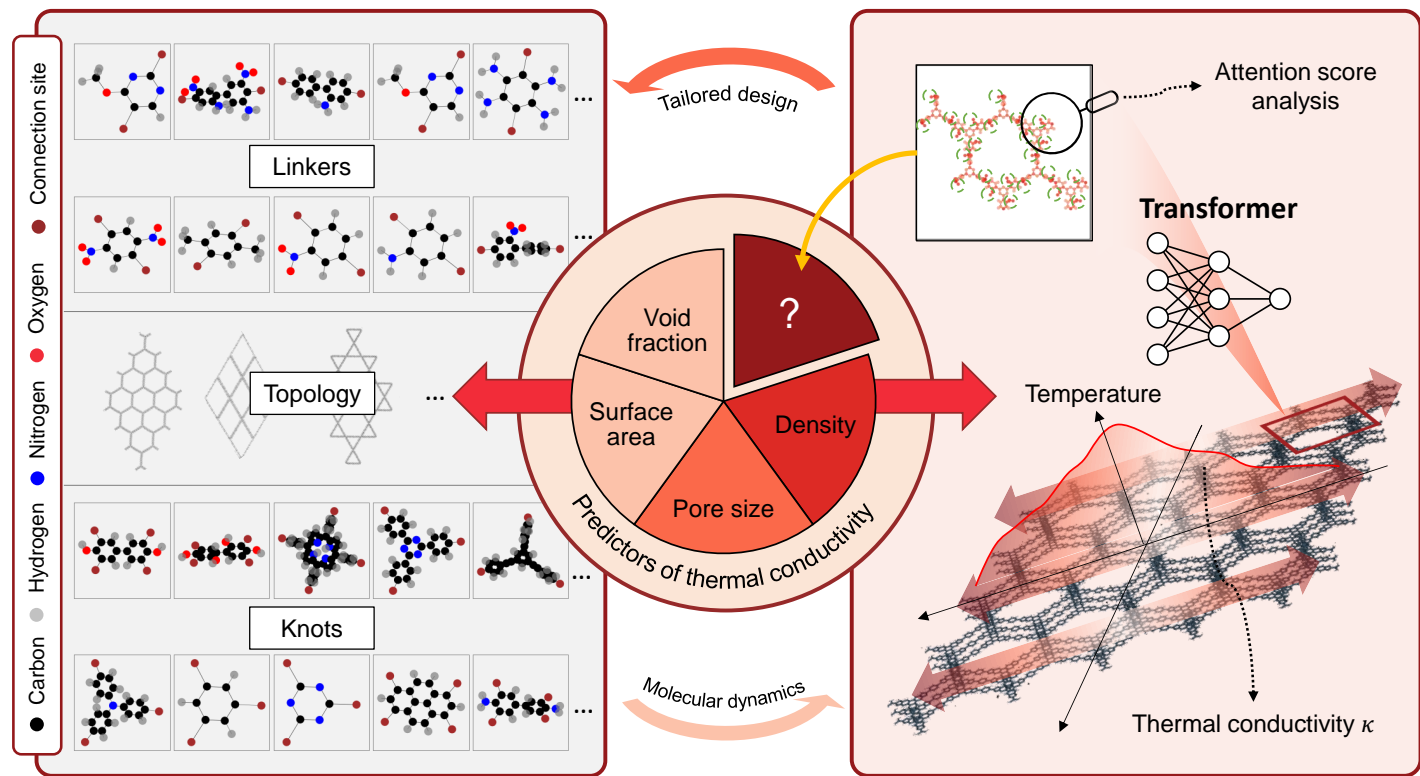


Figure 1: Overview of this study. A COF structure consists of molecular substructures called linkers and knots arranged in a periodic pattern described by the topology. Through molecular dynamics, we construct a large dataset of 2,471 COFs (with diverse linkers, knots, and topologies) and their corresponding thermal conductivities. We demonstrate that conventional descriptors, such as density, pore size, void fraction, and surface area, fail to predict the thermal conductivity reliably. We employ a machine learning framework based on attention mechanism and transformer architecture to uncover a novel predictor, thus enhancing our understanding of the structure-property relationship of thermal conductivity of COFs.

advances in computing hardware, even virtual screening can be prohibitively inefficient for a large design space. This is highlighted by the example that generating a dataset of just 2,471 two-dimensional COFs and their thermal conductivity for this study required 1.3 million CPU-hours in cloud computing (translating into approximately four months and \$70,000 in time and cost, respectively). This underscores the need for efficient structure-property maps that are accurate, generalizable, and interpretable.

Recently, Islamov et al. [32] performed a high-throughput screening study of over 10,000 MOF structures and their thermal conductivity (κ) using MD. They found that the majority of the MOFs possess $\kappa < 1 \text{ W m}^{-1} \text{ K}^{-1}$ with a few exceptions possessing ultra-high thermal conductivity ($\kappa > 10 \text{ W m}^{-1} \text{ K}^{-1}$). While COFs are generally more thermally stable (owing to the strong covalent bonding of the building blocks), a recent study by Thakur et al. [33] on high-throughput screening study on over 10,000 COFs demonstrated that, generally, COFs also possess a similar range of κ , with the majority of the structures exhibiting $\kappa < 1 \text{ W m}^{-1} \text{ K}^{-1}$. Interestingly, MOFs and COFs possess similar structure-property trends. (i) Increasing the pore size is mostly sufficient to achieve a low thermal conductivity. (ii) Additionally, one can increase the void fraction, the surface area, or include heavy atoms to further decrease thermal conductivity. (iii) However, to increase the thermal conductivity, there are many factors that need to align. Islamov et al. [32] demonstrated that while lowering the pore size and increasing the density results in a higher ceiling of attainable thermal conductivity, other factors, such as the topology, mass-mismatch, and linker length also need to be accounted for. Thakur et al. [33] came to similar conclusions alongside the observation that aligning the polymeric chains in the structure to heat flow direction raises the ceiling of attainable thermal conductivity. However, these hand-crafted guidelines and ad hoc correlations are insufficient for developing an accurate and generalizable predictive model that captures the thermal conductivity structure-property relationships of COFs. Our study shows that no combination of commonly used descriptors consistently predicts thermal conductivity. Consequently, a definitive method for identifying COFs with tailor-made

thermal properties for various applications remains elusive.

To address this knowledge gap, we turn to machine learning (ML) with an emphasis on interpretability and explainability. Previous efforts in ML-assisted design for thermally conductive organic materials include the discovery of polymers with high κ through a hierarchical feature selection process [34], a reinforcement learning approach using SMILES-based representations [35], and methods leveraging molecular fingerprints as input features, such as fine-tuning a pre-trained regression model followed by screening [36], training a neural network [37], and employing an active learning approach [38]. Hu et al. [39] provide a review of recent efforts and outlook on ML for thermally conductive organic materials. For the ML modeling of structure-property maps of porous polymers (including but not limited to COFs) there are primarily two routes:

- *high interpretability, limited accuracy*: using hand-crafted and pre-extracted high-level of the crystalline network (e.g., pore size, density, surface area, atomic composition) as input to classical regression algorithms [40, 41, 42];
- *high accuracy, limited interpretability*: using information-rich but raw graph representation of the crystalline network (where nodes denote atoms with features such as position and atom type, and edges denote bonds with the bond order as the feature) as input to end-to-end deep learning-based regression algorithms [43, 44, 45, 46].

Here, we bridge the two routes to develop an accurate predictive model using deep learning while also combining interpretability insights from deep learning with prior knowledge and descriptors to explain the thermal conductivity structure-property relationships of COFs (see Figure 1 for an overview).

In the following, we first conduct a large-scale data analysis of the thermal conductivity structure-property relations of COFs and identify the deficiencies in commonly used descriptors. Next, we provide a deep learning model that accurately predicts the thermal conductivity of COFs. Subsequently, an analysis of the attention scores of the deep learning model uncovers the presence of dangling atoms in the crystalline network of COFs as a strong and so-far missing key predictor for thermal conductivity. Additional physics-based analysis sheds light on the important role of dangling atoms in lowering the thermal conductivity of COFs by disrupting heat transfer pathways. We close by utilizing the ML model for efficient high-throughput screening and identifying COFs with extreme thermal conductivities.

Results

High-throughput data analysis

We create a labelled dataset of COFs and their thermal conductivities by selecting 2,471 two-dimensional COFs from the unlabelled dataset of Mercado et al. [47] The COF structures in this design space are made up of one type of nodal linker (also referred to as *knot*) and one type of connecting linker. The sampled subset consists of COFs with 104 different linkers arranged in 25 different topologies (e.g., honeycomb, kagome, square lattice, etc.), and bonded by four different types of covalent linkages (i.e., carbon-carbon, amine, amide, and imine). We conduct non-equilibrium molecular dynamics (NEMD) simulations to calculate thermal conductivities in two orthogonal in-plane directions (see Supporting Information Section 1.1 for more details). In Supporting Information Section 1.2, we show that there is minimal in-plane anisotropy in thermal conductivity across the dataset. Therefore, we utilize average thermal conductivity in both directions, denoted as κ , as the quantity of interest to explore the structure-property relationships of COFs. In the following and in Figure 2, we present the observations from data analysis of the key descriptors of COFs and thermal conductivities in our labelled dataset. The distribution of all features and their correlations are detailed in Section 1.3 of the Supporting Information.

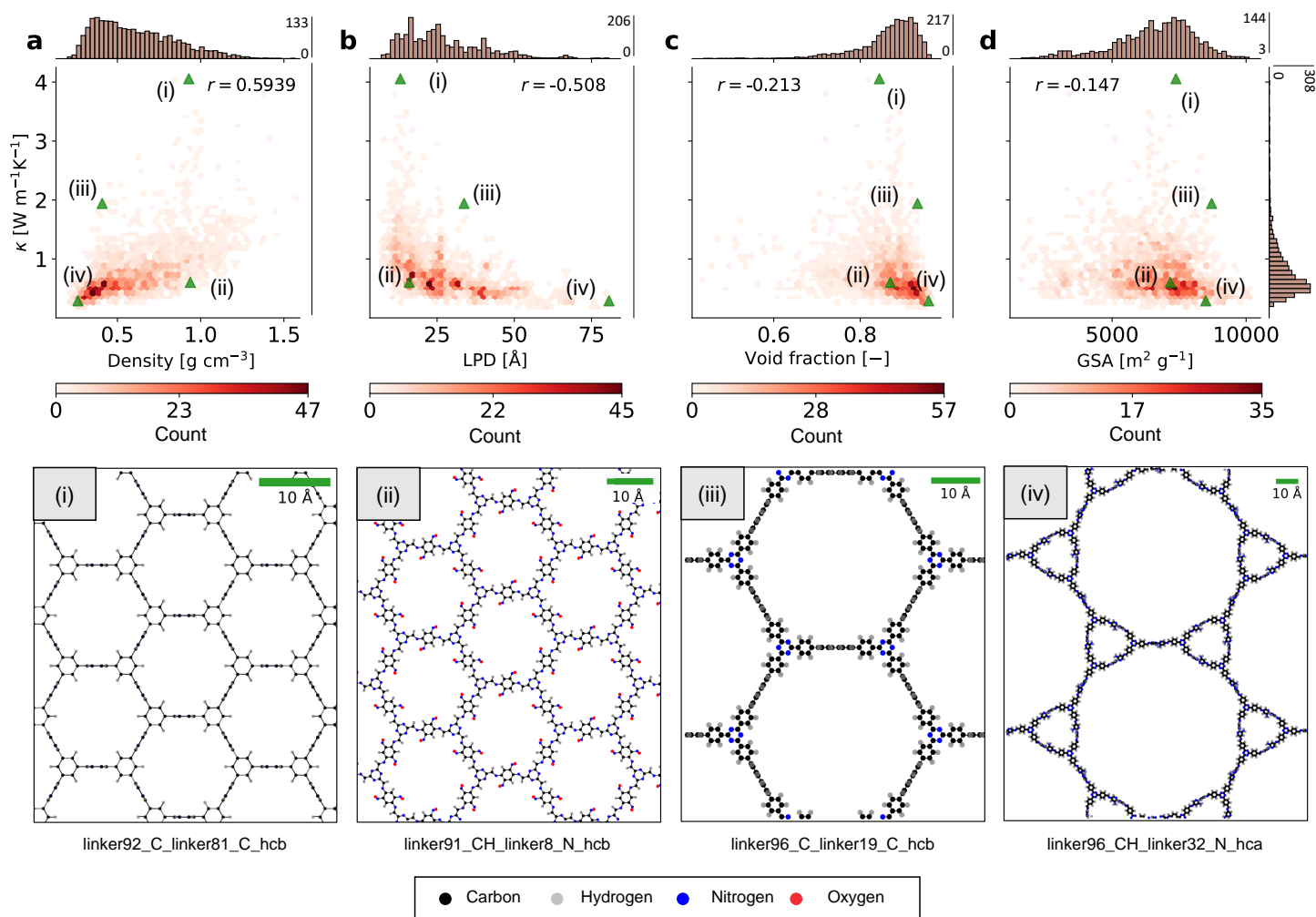


Figure 2: Distribution of (a) κ versus density (with the color indicating data count per bin), (b) κ versus largest pore diameter (LPD), (c) κ versus void fraction, and (d) κ versus gravimetric surface area (GSA). Also shown are four COF structures (i–iv) with contrasting properties, marked by green triangles in the plots above. The r -value indicates the Pearson correlation coefficient.

Density: Figure 2a illustrates the distribution of κ vs. density. There is a large spread of densities within the dataset and the majority of the COFs possess a density of $0.45\text{--}0.55 \text{ g cm}^{-3}$. Moreover, in accordance with previous findings [33], we observe an increasing trend in κ with increasing density. The Pearson correlation coefficient between κ and density is $r = 0.594$, suggesting a moderate positive relationship. However, increasing the density increases the ceiling of attainable κ , but does not guarantee a high value.

Pore size: The pore size of any COF is represented by the largest pore diameter (LPD). Figure 2b shows that LPD in the dataset is spread over a large range between 5 \AA and 80 \AA and a concentration of structures in the $15\text{--}25 \text{ \AA}$ region. Moreover, there is an inverse relationship between the pore size and the thermal conductivity, as previously discovered by Freitas et al. [48], where the range of achievable κ decreases significantly with increasing pore sizes. This is evidenced by the correlation coefficient $r = -0.508$, indicating a moderate negative correlation. Here again, a small pore size does not guarantee a high thermal conductivity. On the other hand, the pore size can be taken as the sole design parameter to effectively reduce the thermal conductivity range (as mentioned in refs. [33, 32]).

Void fraction: Figure 2c shows that the distribution of the void fractions of COFs across the dataset are within the $0.5\text{--}0.96$ range, with the biggest share of COFs possessing a void fraction of around 0.85 and higher. Furthermore, a high void fraction of around 0.85 delivers both the largest values and range of attainable κ within our dataset. This finding is counterintuitive. Void fraction is typically inversely corre-

lated with density (see Supporting Information Section 1.3). Although low density is generally associated with a low κ value, as shown in Figure 2a, the unexpected observation is that a high void fraction (which corresponds to low density) surprisingly results in a high κ value, as also depicted in Figure 2c. Beyond a favorable range of void fractions, no distinct trend emerges in the relationship with κ , as the correlation coefficient $r = -0.213$ suggests only a weak negative relationship.

Surface area: Gravimetric surface area (GSA), i.e., surface area per unit mass varies highly across all the COF structures (see Figure 2d) with a larger cluster of points in the $7000\text{--}8000\text{ m}^2\text{ g}^{-1}$ range. We also observe that around intermediate GSA of $7,000\text{ m}^2\text{ g}^{-1}$, we have the widest spread and highest values of κ . The correlation coefficient of $r = -0.147$ indicates a very weak negative relationship, suggesting that GSA is not a significant predictor.

From the above initial analysis, we notice that the geometrical descriptors used here are insufficient to provide solid trends with respect to thermal conductivity. For example, with all the optimal descriptor values, i.e., a large density, a low pore size, a large void fraction, and an intermediate GSA, we are still not guaranteed to obtain a COF with a high κ . To elucidate this further, we choose four COFs – denoted by (i)–(iv) – and compare them in Figure 2a–d.

COF (i) has the highest thermal conductivity in the dataset with $\kappa = 4.025\text{ Wm}^{-1}\text{K}^{-1}$. The structure has a relatively small pore size with 13.71 \AA (see Figure 2a), a medium density with 0.928 g cm^{-3} (see Figure 2b), a relatively high void fraction of 0.844 (see Figure 2c), and an intermediate surface area of $7381\text{ m}^2\text{g}^{-1}$. In contrast, the second COF (ii) possesses a similar pore size of 9.88 \AA , a similar density of 0.938 g cm^{-3} , a similar void fraction of 0.869 , and a similar surface area of $7171\text{ m}^2\text{g}^{-1}$, but exhibits thermal transfer capabilities almost seven times lower than that of (i) with $\kappa = 0.603\text{ Wm}^{-1}\text{K}^{-1}$.

The third COF (iii) has a pore size of 33.73 \AA in the intermediate-to-high range, a low density at 0.408 g cm^{-3} , a high void fraction at 0.932 , and a slightly larger surface area of $8741\text{ m}^2\text{g}^{-1}$. Following the trends described in literature [33, 48, 49], the geometrical descriptors are not optimal for a high κ . Nonetheless, COF (iii) has rather high $\kappa = 1.96\text{ Wm}^{-1}\text{K}^{-1}$. Lastly, COF (iv) has an exceptionally high pore size at 80.68 \AA and a low density of 0.262 g cm^{-3} but high void fraction of 0.958 . Due to the extreme geometry, the COF (iv) has a very low thermal conductivity of $\kappa = 0.289\text{ Wm}^{-1}\text{K}^{-1}$.

Furthermore, we trained classical ensemble regression models using these descriptors to predict thermal conductivity (detailed results provided in Supporting Information Section 2) and observed that the models yield poor prediction accuracy. This result highlights the limitations of these descriptors in capturing the structure-property relationships underlying thermal conductivity. In summary, the correlation analysis with the previously introduced descriptors and the presented examples illustrate the fact that the thermal conductivity structure-property relationships are complex and call for further examination.

Predicting thermal conductivity using deep learning

Our starting point is the deep learning-based Porous Material Transformer (PMTransformer) developed by Park et al. [46] The PMTransformer is a multi-modal transformer [50] model (see Figure 3 for schematic) designed for universal transfer learning for predicting the properties of porous materials, including COFs, MOFs, and zeolites. It receives two distinct sets of inputs: local and global features. Local features, which reflect the chemistry of building blocks and bonds, are derived from a crystal graph convolutional neural network [51] (CGCNN). The CGCNN directly processes the crystal graph, where atoms and bonds are nodes and edges, respectively, and generates embeddings that capture essential chemical details. These embeddings serve as local features in the PMTransformer. Conversely, global features describe crystalline characteristics, including topological and geometric descriptors such as pore size and surface area. These features are derived from three-dimensional energy grids, which are generated by calculating the interaction energy between the material structure and a methane gas molecule at each grid point using the package GRIDAY [52]. Similar to images in Vision Transformers [53], the energy grids are divided into patches and flattened through linear projections. Eventually, both local and global embeddings are input into a

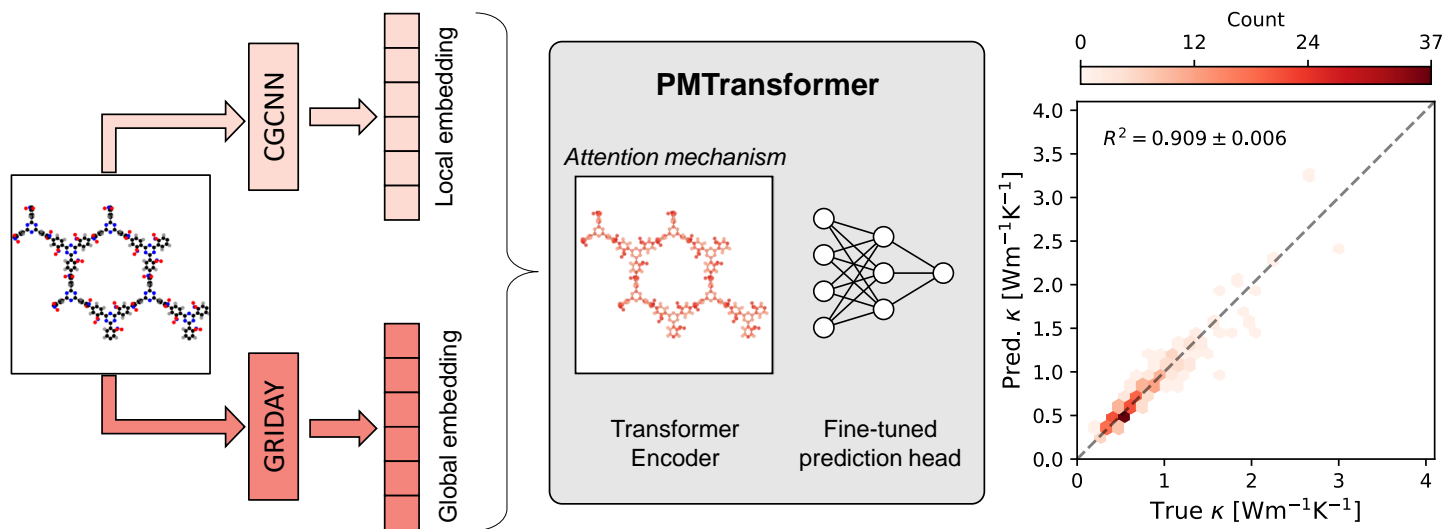


Figure 3: Schematic of PMTransformer model. A sample COF structure is shown on the left. A crystal graph convolutional neural network computes local embeddings of the COF graph, while GRIDAY computes a three-dimensional energy grid of the structure, which becomes the global embeddings. These embeddings are combined and input into the PMTransformer (which includes a transformer encoder with attention mechanism and a prediction head) to predict κ . On the right, a parity plot compares κ predictions with ground truth values. The dashed line represents the ideal line with zero intercept and unit slope.

transformer encoder, where the attention mechanism [50] helps the model focus on the most relevant parts of the molecular structure for predicting (in our case) the thermal conductivity.

To enable universal transfer learning, the transformer encoder in PMTransformer is pre-trained on an extremely large dataset of 1.9 million hypothetical porous materials to predict easily obtainable yet essential properties such as topology, void fraction, and building block prediction. This approach ensures the encoder captures critical information necessary for accurately predicting other, more complex properties in downstream tasks with much smaller datasets. For more details regarding the pre-training of PMTransformer, refer to [46].

In this study, we leveraged the pre-trained transformer encoder of the PMTransformer model to perform transfer learning for the prediction of the thermal conductivity of COFs. We fine-tune the transformer encoder model using the pre-trained weights as a starting point and jointly train a prediction head based on a multi-layer perceptron architecture to map the output of the transformer encoder to the thermal conductivity of COFs. We used the mean squared error (MSE) as a loss function for training. The dataset of 2,471 COFs is randomly split into two subsets: 90% of the data is used for training (out of which 10% for validation), and the remaining data is used for testing. Additional details of the training protocol are provided in Supporting Information Section 3.

We demonstrate the model's prediction accuracy on the test dataset in Figure 3, where it achieves a goodness-of-fit R^2 of 0.909 ± 0.006 (across five random seeds) and a mean absolute error (MAE) of $0.075 \text{ Wm}^{-1}\text{K}^{-1}$ for predicting κ . The model's strong performance suggests that there may be gaps in the feature sets typically used to describe COFs. It also highlights the possibility that additional key descriptors, beyond those commonly used, could play an important role in predicting thermal conductivity, thus warranting further exploration of structure-property relationships.

Discovering novel thermal transfer mechanisms via self-attention

We leverage the multi-head self-attention mechanism [50] of the transformer architecture to interpret the predictions made by the deep learning model. The attention mechanism in transformers is designed to identify and assign weights, known as attention scores, to the significance of different parts of the input

data/encodings relative to all the other parts. When applied to molecular structures, such as COFs, the attention mechanism enables the model to dynamically focus attention on key molecular substructures in relation to all the other substructures present based on their relevance to the property being predicted, in this case, thermal conductivity. In multi-head attention, multiple attention heads are needed to capture different aspects or relationships within the data simultaneously. Specifically, in the context of the PM-Transformer model applied to a COF to predict its thermal conductivity, we calculate the attention for each atom in the COF by averaging the attention scores from all attention heads and computing the joint attention via multiplicative aggregation across all layers of the transformer encoder.

Additionally, we identify the *main branch* of a COF as the shortest continuous path connecting the boundary points necessary for periodicity. We then classify all the atoms extending and excluded from the main branch as *dangling mass*. More details on how we classify each atom as either part of the main branch or part of a dangling side branch are presented in Supporting Information Section 4. We observe distinct patterns in the attention assigned to various atomic sites within a COF's graph representation, which correspond to the location of the dangling masses. Two representative examples are shown in Figure 4.

Consider the first example (see Figure 4a-b). The top row illustrates a COF structure (Figure 4a) from the test dataset with a thermal conductivity of $1.105 \text{ Wm}^{-1}\text{K}^{-1}$ and no dangling masses except hydrogen atoms. Additionally, the atom-wise attention scores are uniformly distributed and low for all the carbon atoms with some elevated attention to the nitrogen atoms. In the second row, we illustrate a COF structure (Figure 4b) with the same topology as the previous one, but with a much lower thermal conductivity of $0.533 \text{ Wm}^{-1}\text{K}^{-1}$. Its attention profile reveals that certain atom groups are being paid special attention to by the transformer, i.e., specifically the $-\text{NO}_2$ functional group on the benzene ring that is dangling from the main branch of the COF. Notably, the same groups of atoms that exhibit higher attention scores are also classified as dangling masses (see Figure 4b attention profile & dangling mass).

In the second example (Figure 4c-d), the COF structure on the top does not contain any dangling mass except hydrogen atoms and has a thermal conductivity of $2.715 \text{ Wm}^{-1}\text{K}^{-1}$ with a highly uniform attention profile (see Figure 4a). Analogously, we pick a second COF structure with the same topology and comparable geometrical descriptors. Once more, we observe that the second structure contains a significant amount of dangling mass (i.e., $-\text{CN}$ branches extending from the rings) with corresponding elevated attention scores and has a lower thermal conductivity of $1.611 \text{ Wm}^{-1}\text{K}^{-1}$.

The same trend is observed for numerous examples, with additional ones presented in the Supporting Information Section 5. We conclude that this increased attention is indicative of the deep learning model's understanding that these dangling masses are significant in predicting thermal conductivity. Furthermore, it suggests that the presence of dangling masses disrupts the heat transfer pathways and thereby reduces the thermal conductivity through the material. A similar effect of dangling mass lowering the thermal conductivity has been reported previously in singular polymer chains [54] and amorphous polymers [55], but remains a novel predictor for COFs which are ordered polymeric structures.

To further validate the structure-property relationship interpreted from the deep learning model, we examine the impact of dangling atoms on the vibrational density of states (VDOS) for the aforementioned contrasting COF examples. VDOS, which characterizes the distribution of vibrational modes in a system as a function of frequency, is known to impact thermal transfer properties. Overlaps in VDOS profiles between different atoms have been shown to affect these properties in both COFs [56] and MOFs [57].

Through MD simulations, the VDOS is calculated using the Fourier transform of the normalized velocity autocorrelation function of specific groups of atoms (see Supporting Information Section 6 for details). Figure 4 (third column) show the VDOS profile of carbon, nitrogen, and oxygen atoms in the representative COF examples. For any COF, we define a VDOS overlap metric S as the ratio of the area under the curve (AUC) of the minimum VDOS across all atom types (at each frequency) and the AUC of the maximum

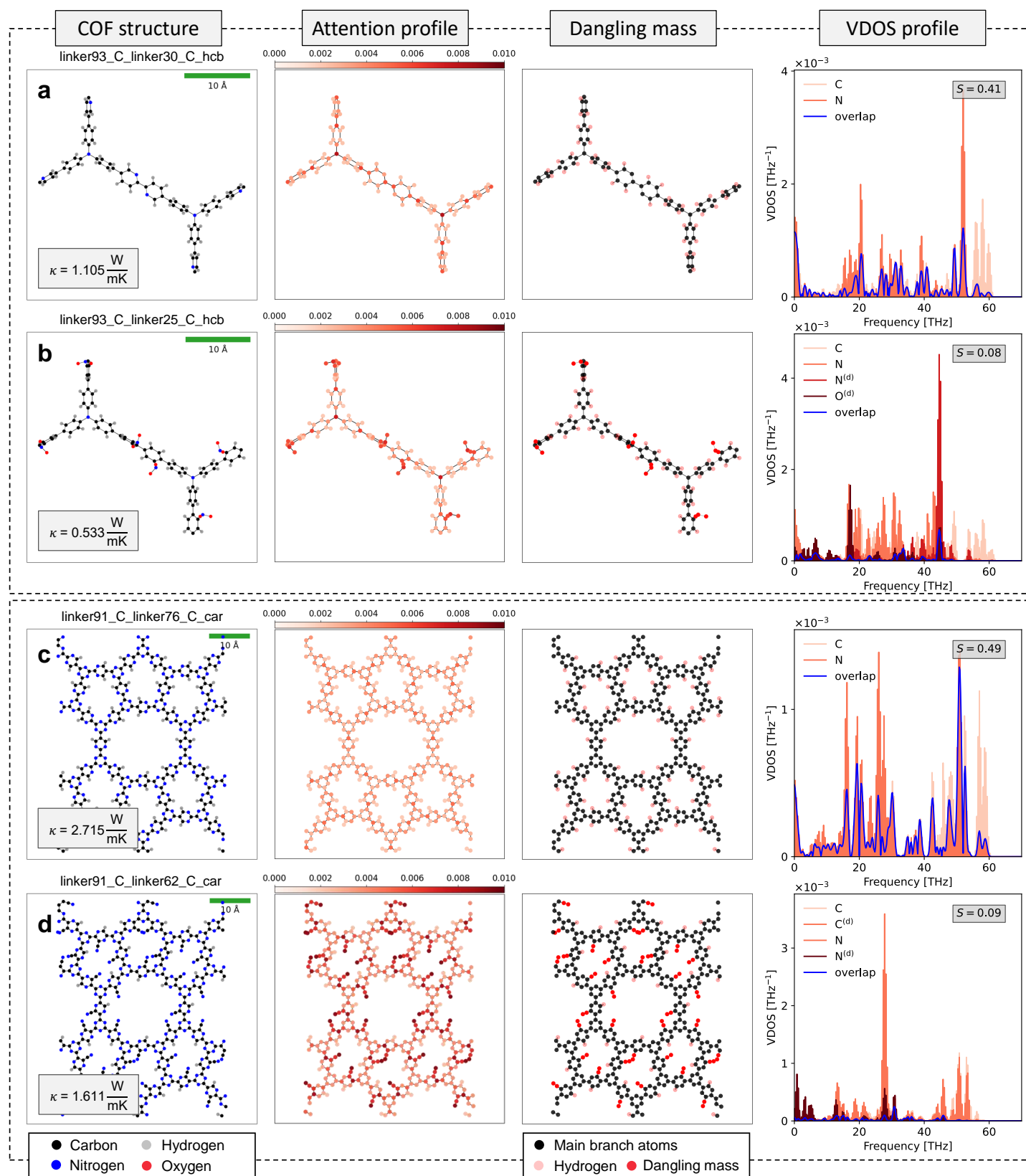


Figure 4: Two example pairs (contained in dashed boxes) of COFs with same topologies, similar geometric descriptors, but contrasting thermal conductivities. The first column illustrates the COF structures. The second column shows the atom-level attention score profile computed by the attention mechanism. The third column shows the same COF structure distinguishing atoms on the main branch and dangling atoms (with separate distinction for hydrogen atoms). The fourth column shows the VDOS profiles of various groups of atoms within the corresponding COF structure with the overlap metric S . The legend indicates the VDOS profile for main branch atoms (.) and dangling atoms (.)^(d).

VDOS across all atom types (at each frequency), i.e.,

$$S = \frac{\int_{\omega} \min \left\{ f_C^V(\omega), f_N^V(\omega), f_O^V(\omega), f_B^V(\omega), f_C^{V,d}(\omega), f_N^{V,d}(\omega), f_O^{V,d}(\omega), f_B^{V,d}(\omega) \right\} d\omega}{\int_{\omega} \max \left\{ f_C^V(\omega), f_N^V(\omega), f_O^V(\omega), f_B^V(\omega), f_C^{V,d}(\omega), f_N^{V,d}(\omega), f_O^{V,d}(\omega), f_B^{V,d}(\omega) \right\} d\omega}. \quad (1)$$

Here, ω denotes the frequency; $f_C^V(\omega)$, $f_N^V(\omega)$, $f_O^V(\omega)$, and $f_B^V(\omega)$ denote the VDOS at frequency ω for the carbon, nitrogen, oxygen and boron atoms, respectively. Additionally, we differentiate between atoms in the main branch and dangling atoms, where the VDOS profiles for dangling atoms are denoted with a $(.)^d$ superscript. A large overlap in VDOS profiles of different atom types would result in $S \approx 1$, whereas a small overlap would yield $S \approx 0$. A high overlap indicates that phonon waves (i.e., quantized modes of vibrations responsible for thermal energy transfer within the crystal lattice) can propagate freely throughout the structure. This would lead to minimized phonon scattering and facilitate efficient heat transfer across the material [58].

In the COF structures, which lack or have minimal dangling atoms, the VDOS profiles of the atoms are broad and overlap significantly, e.g., $S \approx 0.41$ and 0.49 for examples in Figure 4a and c, respectively. This results in an even distribution of vibrational modes across a wide frequency spectrum for all atoms. In contrast, the COFs with substantial dangling atoms exhibit a VDOS profile with minimal overlap, e.g., $S \approx 0.08$ and 0.09 for examples in Figure 4b and d, respectively. The vibrational modes of individual atoms in these COFs are confined to much narrower frequency bands, which leads to a less harmonized VDOS profile. The lack of overlap suggests that the vibrations are highly localized around the dangling atoms, which causes the phonon waves to be scattered and disrupting their ability to transfer heat efficiently through the material [59]. We interpret the mismatch in the VDOS profiles as an energy barrier for phonon transport, where phonons encounter resistance, preventing smooth energy transfer across atoms. This suggests that the absence of dangling mass is crucial for enhancing thermal conductivity in COFs. Dangling atoms create these mismatches in VDOS, which in turn hinders phonon transport and reduces thermal conductivity.

To further confirm the effect of dangling atoms on phonon dispersion in COFs, we calculate the phonon spectral energy density (pSED) of the example COFs and their dangling counterparts, as presented in Section 5 in Supporting Information. The pSED of COFs containing more dangling atoms exhibits higher magnitudes and broadening bands, indicating stronger anharmonicity and vibrational scattering in the vibrational modes, consequently resulting in reduced thermal conductivity [60].

To quantify the role of dangling masses in the structure-property relationship for thermal conductivity of COFs, we introduce the dangling mass ratio (DMR). The $\text{DMR} \in [0, 1]$ quantifies the ratio between the mass of dangling atoms and the total mass of the COF, i.e.,

$$\text{DMR} = \frac{\sum_{i \in \mathcal{D}} m_i}{\sum_{i \in \mathcal{D}} m_i + \sum_{i \in \mathcal{M}} m_i}, \quad (2)$$

where m_i is the mass of the i^{th} atom belonging to the set of either dangling atoms or of non-dangling main branch atoms – denoted by \mathcal{D} and \mathcal{M} , respectively. Higher DMR values indicate a greater proportion of dangling masses relative to the COF's total mass.

We then introduce DMR as an additional feature, alongside pore size, density, void fraction, and surface area, and train classical ensemble regression models, such as the Random Forest [61], Gradient Boosting [62], XGBoost [63], and AdaBoost [64] and outline their performances in Table 1. To assess the importance of individual features, including DMR, we analyzed their Gini importance and conducted a permutation feature importance analysis [65]. These values quantify the contribution of each feature to the overall predictive power of the model. The Gini importance measures how much each feature reduces the Gini impurity or randomness when making predictions in the ensemble model [61]. On the other hand, permutation feature importance measures the impact of a feature by assessing how much the model's performance decreases when the values of that feature are randomly shuffled. A greater drop in performance indicates

Regression Model	R^2
Random Forest	0.728 ± 0.069
Gradient Boosting	0.688 ± 0.070
XGBoost	0.691 ± 0.035
AdaBoost	0.416 ± 0.125

Table 1: Performances of standard ensemble regression models at predicting κ by including DMR as an input feature. The table reports R^2 scores obtained through 10-fold cross-validation.

Feature importances for Random Forest

Feature	Gini	PFI
Density	0.397	0.670
DMR	0.278	0.511
LPD	0.185	0.455
Void Fraction	0.070	0.093
Surface Area	0.069	0.022

Table 2: Feature importances for the best-performing regression model, i.e., Random Forest. The table reports both Gini and Permutation Feature Importance (PFI) values for all features.

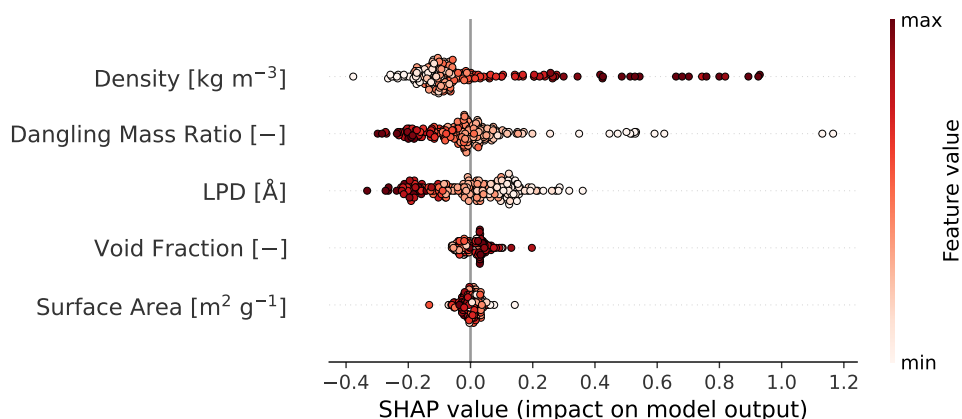


Figure 5: Distribution of the effect of each feature on the model’s predictions. Each point represents a SHAP value for a feature across all samples, with the color intensity indicating feature values (ranging between minimum and maximum values). The position along the x-axis represents the magnitude of the feature’s impact.

that the feature is more important in predicting the target variable [61]. We note that for the best performing regressor, the Random Forest, DMR emerges as the second most influential predictor with 27.8% Gini importance, closely following behind density (see Table 2). Similarly, the permutation feature importance analysis also highlights DMR as a key feature, further supporting its significant role in predicting thermal conductivity, with its importance consistently ranking just below density. Finally, we conducted SHAP analysis [66] on the the Random Forest to better understand the impact of each feature on the individual test data points. As shown in Figure 5, the analysis reveals that higher DMR values are associated with lower predicted κ , confirming the trend we observed. The consistency of these findings across different methods—Gini, permutation feature importance, and SHAP—reinforces the importance of DMR as a key factor in predicting thermal conductivity.

Generalizability and high-throughput screening for discovering COFs with tailored properties

To evaluate the generalization capabilities of the deep learning model for high-throughput screening, we screen previously unseen 6,170 two-dimensional COFs in the unlabelled dataset by Mercado et al. [47] from which our training and test sets were originally subsampled. Moreover, we screen 35,638 two-dimensional COFs in the unlabelled dataset by Lan et al. [67] This dataset covers a vastly different design space with a variety of linkers and knots previously unseen by our trained model.

The screening is performed with the objective of facilitating the identification COFs with extremely high or low thermal conductivity without resorting to computationally expensive simulations. We observe an average screening rate of 0.07 seconds per COF structure (see Supporting Information Section 7 for details

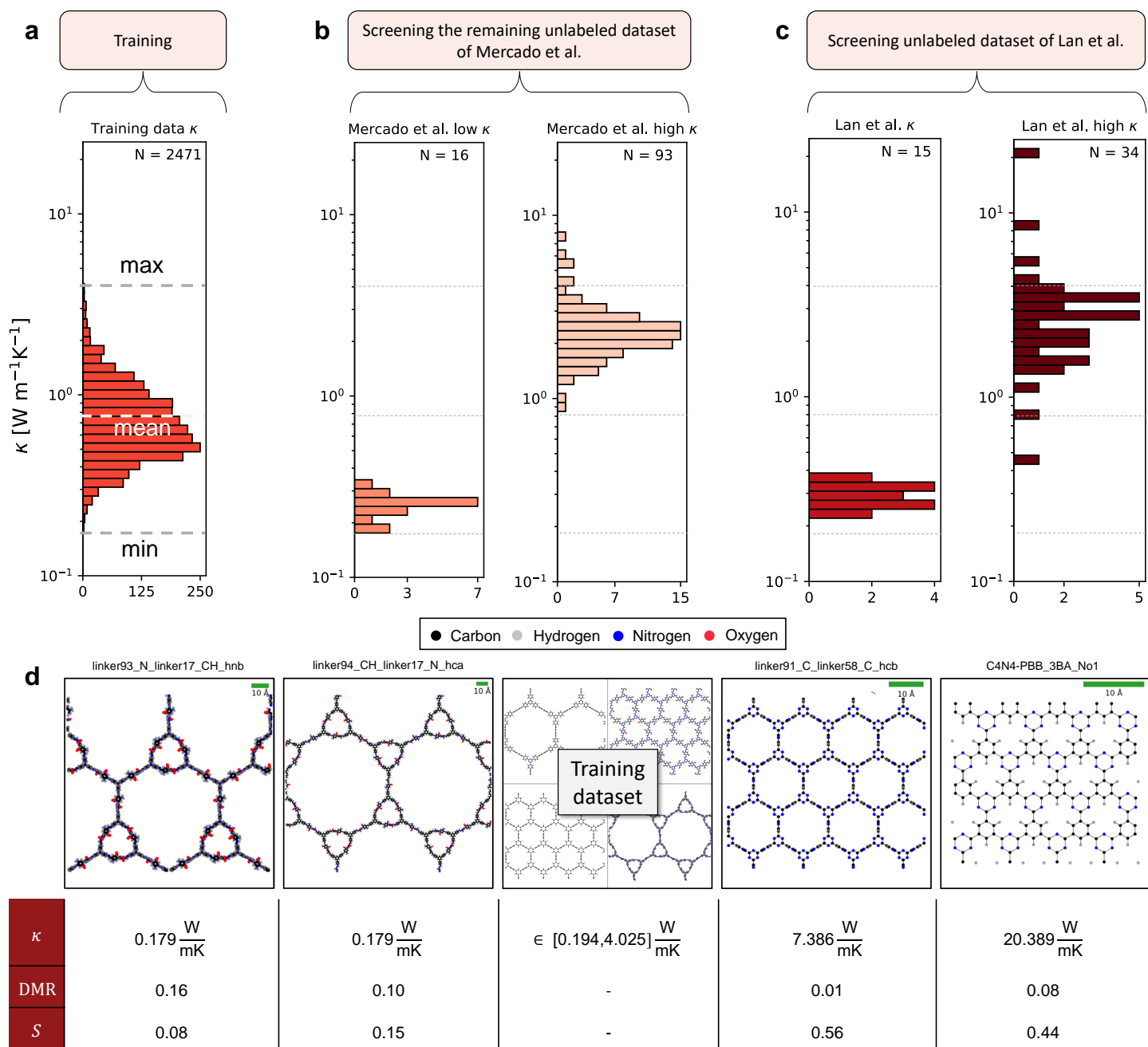


Figure 6: High-throughput screening. (a) Distribution of κ in the training dataset. Dashed lines indicated minimum, mean, and maximum κ across the training dataset. (b,c) Distribution of κ of selected COF candidates identified in high-throughput screening for low and high κ in the unlabeled datasets of (b) Mercado et al. [47] and (c) Lan et al. [67] While the former dataset shares the same design space as the training dataset, the latter has a different design space. All thermal conductivities shown here are computed using MD. (d) Representative COFs identified through high-throughput screening with κ lower and higher than the minimum and maximum, respectively, across the training dataset. Also indicated are their corresponding DMR and S values.

on computational runtimes), thereby enabling a speedup of almost seven orders of magnitude compared to MD-based screening.

Once potential candidates with extreme thermal conductivities are identified using the PMTransformer, we then calculate their thermal conductivities through MD simulations for these selected few, rather than for the entire datasets. The results are summarized in Figure 6. Our screening process on the dataset by Mercado et al. [47] revealed COFs exhibiting thermal conductivities up to twice the maximum value observed in the training set, but stemming from the same design space. By screening the dataset by Lan et al. [67], we discover COFs with thermal conductivities five times as high as the ones in our training

set. Additionally, we discovered several COFs with thermal conductivities lower than any values previously recorded in our dataset. A visual inspection reveals that these COFs feature a combination of large pore sizes, low density, and a substantial presence of dangling masses. For all the identified COFs, we observe that thermal conductivity shows a strong trend with both dangling mass ratio (DMR) and VDOS overlap ratio (S), which is in agreement with the previous observations.

Discussion

In this study, we compiled an extensive dataset of thermal conductivities for 2,471 two-dimensional COFs, computed using NEMD. Despite observing some structure-property trends with conventional descriptors such as density, pore size, void fraction, and surface area, no single descriptor or combination thereof consistently predicted thermal conductivity with high accuracy, highlighting the complexity of COF structure-property relationships. To enhance prediction accuracy, we trained a transformer-based deep learning model incorporating a multi-head attention mechanism. This model significantly outperformed traditional ensemble regression models, achieving an R^2 of 0.909 ± 0.006 .

Further analysis using the transformer's attention mechanism revealed that COFs with higher amounts of dangling atoms exhibited lower thermal conductivities due to disrupted heat transfer pathways, identifying a novel and significant predictor of thermal conductivity. The random forest regressor, identified as the best-performing regression ensemble model, was analyzed using Gini importance, permutation feature importance, and SHAP values. These analyses consistently highlighted the dangling mass ratio as the second most important predictor of thermal conductivity. The vibrational density of states analysis further supported these findings, showing that dangling masses introduce mismatched vibrational modes that hinder thermal transfer.

We further leveraged the deep learning model to efficiently screen thousands of COFs, both within and beyond the design space we analyzed, to identify candidates with extreme thermal conductivities. This approach provides a rapid and reliable method as well as valuable insights for designing COFs with tailored thermal characteristics. To support further research, we release the dataset of COF thermal conductivities and encourage the research community to utilize and expand upon it. Finally, we emphasize the need to bridge high interpretability with high accuracy in machine learning models to navigate the complex structure-property space of COFs and other nanoporous materials, thereby enabling the design of optimal materials for applications such as gas separation and thermal management.

Methods

The molecular dynamics setup, the distribution of in-plane thermal conductivities, and feature correlations (including DMR) (Section 1); implementation details of the ensemble regression models and regression performances excluding DMR (Section 2); the deep learning setup (Section 3); the dangling mass computation (Section 4); additional comparisons of COFs with and without dangling mass, including phonon dispersion maps for all examples (Section 5); details on the VDOS and pSED computation (Section 6); and estimated runtimes (Section 7) are summarized in the Supporting Information.

Acknowledgements

P.T., Y.G., and S.K. acknowledge that this material is based upon work supported by the Air Force Office of Scientific Research under award number FA8655-23-1-7020. P.T., Y.G., and S.K. acknowledge that this work was supported in part by Oracle Cloud credits and related resources provided by Oracle for Research. A.V. and Y.Z. acknowledge Microsoft Climate Research Initiative and University of Washington

for funding. The funders played no role in study design, data collection, analysis and interpretation of data, or the writing of this manuscript.

We thank Prof. Marcel Sluiter of TU Delft for his helpful discussions and insights during the course of this research. Additionally, we thank Eric Vo of University of Washington for his help in preparing simulations of COF structures.

Competing interests

The authors declare no competing interests.

Data availability

The datasets generated during the current study are available at <link will be provided at time of publication>.

Code availability

The codes generated during the current study are available at <link will be provided at time of publication>.

References

- [1] H. Wang, H. Wang, Z. Wang, L. Tang, G. Zeng, P. Xu, M. Chen, T. Xiong, C. Zhou, X. Li, D. Huang, Y. Zhu, Z. Wang, J. Tang, *Chemical Society Reviews* **2020**, *49*, 12 4135–4165.
- [2] X. Zhao, P. Pachfule, A. Thomas, *Chemical Society Reviews* **2021**, *50*, 12 6871–6913.
- [3] C. Liu, J. Wang, J. Wan, C. Yu, *Coordination Chemistry Reviews* **2021**, *432* 213743.
- [4] N. Stock, S. Biswas, *Chemical Reviews* **2011**, *112*, 2 933–969.
- [5] E. Pérez-Botella, S. Valencia, F. Rey, *Chemical Reviews* **2022**, *122*, 24 17647–17695.
- [6] H. R. Abuzeid, A. F. EL-Mahdy, S.-W. Kuo, *Giant* **2021**, *6* 100054.
- [7] M. Dogru, M. Handloser, F. Auras, T. Kunz, D. Medina, A. Hartschuh, P. Knochel, T. Bein, *Angewandte Chemie International Edition* **2013**, *52*, 10 2920–2924.
- [8] L. Stegbauer, S. Zech, G. Savasci, T. Banerjee, F. Podjaski, K. Schwinghammer, C. Ochsenfeld, B. V. Lotsch, *Advanced Energy Materials* **2018**, *8*, 24.
- [9] Z. Ali, T. Huo, Y. Zhang, G. Wang, *Microchemical Journal* **2024**, *200* 110340.
- [10] Y. Li, M. Chen, Y. Han, Y. Feng, Z. Zhang, B. Zhang, *Chemistry of Materials* **2020**, *32*, 6 2532–2540.
- [11] Y. Yusran, H. Li, X. Guan, Q. Fang, S. Qiu, *EnergyChem* **2020**, *2*, 3 100035.
- [12] M. C. Scicluna, L. Vella-Zarb, *ACS Applied Nano Materials* **2020**, *3*, 4 3097–3115.
- [13] H. Guo, Y. Liu, N. Wu, L. Sun, W. Yang, *ChemistrySelect* **2022**, *7*, 34.
- [14] L. Wang, B. Dong, R. Ge, F. Jiang, J. Xu, *ACS Applied Materials & Interfaces* **2017**, *9*, 8 7108–7114.

- [15] Y. Chumakov, F. Aksakal, A. Dimoglo, A. Ata, S. A. Palomares-Sánchez, *Journal of Electronic Materials* **2016**, *45*, 7 3445–3452.
- [16] S. Wang, X. Xu, Y. Yue, K. Yu, Q. Shui, N. Huang, H. Chen, *Small Structures* **2020**, *1*, 2.
- [17] H. Fan, A. Mundstock, A. Feldhoff, A. Knebel, J. Gu, H. Meng, J. Caro, *Journal of the American Chemical Society* **2018**, *140*, 32 10094–10098.
- [18] M.-X. Wu, Y.-W. Yang, *Chinese Chemical Letters* **2017**, *28*, 6 1135–1143.
- [19] X. Zhou, Y. Yan, X. Lu, H. Zhu, X. Han, G. Chen, Z. Ren, *Materials Today* **2018**, *21*, 9 974–988.
- [20] A. M. Evans, M. R. Ryder, W. Ji, M. J. Strauss, A. R. Corcos, E. Vitaku, N. C. Flanders, R. P. Bisbey, W. R. Dichtel, *Faraday Discussions* **2021**, *225* 226–240.
- [21] X. Zou, H. Ren, G. Zhu, *Chemical Communications* **2013**, *49*, 38 3925.
- [22] Z.-F. Pang, T.-Y. Zhou, R.-R. Liang, Q.-Y. Qi, X. Zhao, *Chemical Science* **2017**, *8*, 5 3866–3870.
- [23] B. Gui, G. Lin, H. Ding, C. Gao, A. Mal, C. Wang, *Accounts of Chemical Research* **2020**, *53*, 10 2225–2234.
- [24] X. Xu, J. Chen, J. Zhou, B. Li, *Advanced Materials* **2018**, *30*, 17.
- [25] C. Choy, *Polymer* **1977**, *18*, 10 984–1004.
- [26] K. Utimula, T. Ichibha, R. Maezono, K. Hongo, *Chemistry of Materials* **2019**, *31*, 13 4649–4656.
- [27] L. Lindsay, D. A. Broido, T. L. Reinecke, *Phys. Rev. Lett.* **2012**, *109* 095901.
- [28] A. H. Romero, E. K. U. Gross, M. J. Verstraete, O. Hellman, *Phys. Rev. B* **2015**, *91* 214310.
- [29] H. Li, J.-L. Brédas, *Chemistry of Materials* **2021**, *33*, 12 4529–4540.
- [30] Z. Li, Z. Liu, Z. Li, T. Wang, F. Zhao, X. Ding, W. Feng, B. Han, *Advanced Functional Materials* **2020**, *30*, 10.
- [31] D. C. Rapaport, *The Art of Molecular Dynamics Simulation*, Cambridge University Press, **2004**.
- [32] M. Islamov, H. Babaei, R. Anderson, K. B. Sezginel, J. R. Long, A. J. H. McGaughey, D. A. Gomez-Gualdron, C. E. Wilmer, *npj Computational Materials* **2023**, *9*, 1.
- [33] S. Thakur, A. Giri, *Small* **2024**, *20*, 32.
- [34] X. Huang, S. Ma, C. Y. Zhao, H. Wang, S. Ju, *npj Computational Materials* **2023**, *9*, 1.
- [35] R. Ma, H. Zhang, T. Luo, *ACS Applied Materials & Interfaces* **2022**, *14*, 13 15587.
- [36] S. Wu, Y. Kondo, M.-a. Kakimoto, B. Yang, H. Yamada, I. Kuwajima, G. Lambard, K. Hongo, Y. Xu, J. Shiomi, et al., *Npj Computational Materials* **2019**, *5*, 1 66.
- [37] K. Ishikiriya, *Thermochimica Acta* **2022**, *708* 179135.
- [38] J. Xu, T. Luo, *npj Computational Materials* **2024**, *10*, 1 74.
- [39] Y. Hu, Q. Wang, H. Ma, *Journal of Applied Physics* **2024**, *135*, 12.
- [40] P. Yang, H. Zhang, X. Lai, K. Wang, Q. Yang, D. Yu, *ACS Omega* **2021**, *6*, 27 17149–17161.
- [41] X. Cao, Z. Zhang, Y. He, W. Xue, H. Huang, C. Zhong, *Industrial & Engineering Chemistry Research* **2022**, *61*, 30 11116–11123.
- [42] J. S. De Vos, S. Ravichandran, S. Borgmans, L. Vanduyfhuys, P. Van Der Voort, S. M. J. Rogge, V. Van Speybroeck, *Chemistry of Materials* **2024**, *36*, 9 4315–4330.

- [43] G. Zhao, Y. G. Chung, *Journal of Chemical Theory and Computation* **2024**, *20*, 12 5368–5380.
- [44] V. Korolev, A. Mitrofanov, *Journal of Chemical Information and Modeling* **2024**, *64*, 6 1919.
- [45] Y. Kang, H. Park, B. Smit, J. Kim, *Nature Machine Intelligence* **2023**, *5*, 3 309–318.
- [46] H. Park, Y. Kang, J. Kim, *ACS Applied Materials & Interfaces* **2023**, *15*, 48 56375–56385.
- [47] R. Mercado, R.-S. Fu, A. V. Yakutovich, L. Talirz, M. Haranczyk, B. Smit, *Chemistry of Materials* **2018**, *30*, 15 5069–5086.
- [48] S. K. S. Freitas, R. S. Borges, C. Merlini, G. M. O. Barra, P. M. Esteves, *The Journal of Physical Chemistry C* **2017**, *121*, 48 27247–27252.
- [49] J. Kwon, H. Ma, A. Giri, P. E. Hopkins, N. B. Shustova, Z. Tian, *ACS Nano* **2023**, *17*, 16 15222–15230.
- [50] A. Vaswani, N. Shazeer, N. Parmar, J. Uszkoreit, L. Jones, A. N. Gomez, L. Kaiser, I. Polosukhin, Attention is all you need, **2017**, URL <https://arxiv.org/abs/1706.03762>.
- [51] T. Xie, J. C. Grossman, *Phys. Rev. Lett.* **2018**, *120* 145301.
- [52] GitHub - Sangwon91/GRIDAY: Energy shape calculator for the porous materials — github.com, <https://github.com/Sangwon91/GRIDAY>, [Accessed 14-06-2024].
- [53] A. Dosovitskiy, L. Beyer, A. Kolesnikov, D. Weissenborn, X. Zhai, T. Unterthiner, M. Dehghani, M. Minderer, G. Heigold, S. Gelly, J. Uszkoreit, N. Houlsby, *arXiv preprint arXiv:2010.11929* **2020**.
- [54] D. Luo, C. Huang, Z. Huang, *Journal of Heat Transfer* **2017**, *140*, 3.
- [55] T. Feng, J. He, A. Rai, D. Hun, J. Liu, S. S. Shrestha, *Phys. Rev. Appl.* **2020**, *14* 044023.
- [56] D. Feng, Y. Feng, Y. Liu, W. Zhang, Y. Yan, X. Zhang, *The Journal of Physical Chemistry C* **2020**, *124*, 15 8386–8393.
- [57] P. Ying, J. Zhang, Z. Zhong, *The Journal of Physical Chemistry C* **2021**, *125*, 23 12991–13001.
- [58] S. Wang, L. Ren, M. Han, W. Zhou, C. Wong, X. Bai, R. Sun, X. Zeng, *Nanoscale* **2023**, *15*, 19 8706–8715.
- [59] P. Ying, J. Zhang, X. Zhang, Z. Zhong, *The Journal of Physical Chemistry C* **2020**, *124*, 11 6274–6283.
- [60] M. A. Rahman, S. Thakur, P. E. Hopkins, A. Giri, *The Journal of Physical Chemistry C* **2023**, *127*, 23 11157.
- [61] L. Breiman, *Machine Learning* **2001**, *45*, 1 5–32.
- [62] J. H. Friedman, *The Annals of Statistics* **2001**, *29*, 5.
- [63] T. Chen, C. Guestrin, In *Proceedings of the 22nd ACM SIGKDD International Conference on Knowledge Discovery and Data Mining*, volume 11 of *KDD '16*. ACM, **2016** 785–794, URL <http://dx.doi.org/10.1145/2939672.2939785>.
- [64] Y. Freund, R. E. Schapire, *Journal of Computer and System Sciences* **1997**, *55*, 1 119–139.
- [65] F. Pedregosa, G. Varoquaux, A. Gramfort, V. Michel, B. Thirion, O. Grisel, M. Blondel, P. Prettenhofer, R. Weiss, V. Dubourg, J. Vanderplas, A. Passos, D. Cournapeau, M. Brucher, M. Perrot, E. Duchesnay, *Journal of Machine Learning Research* **2011**, *12* 2825.
- [66] S. Lundberg, *arXiv preprint arXiv:1705.07874* **2017**.
- [67] Y. Lan, X. Han, M. Tong, H. Huang, Q. Yang, D. Liu, X. Zhao, C. Zhong, *Nature Communications* **2018**, *9*, 1.

Deep learning reveals key predictors of thermal conductivity in covalent organic frameworks

Supporting Information

Prakash Thakolkaran^{1,†} Yiwen Zheng^{2,†} Yaqi Guo¹ Aniruddh Vashisth^{2,*} Siddhant Kumar^{1,*}

¹Department of Materials Science and Engineering, Delft University of Technology, 2628 CD Delft, The Netherlands

²Department of Mechanical Engineering, University of Washington, Seattle, WA, USA

*Equal contribution

[†]Email: vashisth@uw.edu, sid.kumar@tudelft.nl; equal contribution

1 Data generation

1.1 Molecular Dynamics

We carry out MD simulations on two-dimensional COF structures sampled from the unlabeled dataset by Mercado et al. [1] to calculate their in-plane thermal conductivities. The simulations are performed by Large-scale Atomic/Molecular Massively Parallel Simulator (LAMMPS) [2]. We employ the Dreiding force field [3] to describe the interatomic interactions due to its applicability to a wide range of 2D COFs with various chemistries and topologies, as well as compatibility with the unit cell structures from the Mercado dataset [1] which were minimized using Dreiding. Other force fields such as reactive potentials fall short in accommodating more than 2,400 COFs in this study due to limited generalizability and high computational cost [4, 5, 6]. The electrostatic interactions between atoms are ignored due to the high computational cost and minimal effect on calculated thermal conductivity of COFs, which is confirmed by the good agreement between the calculated thermal conductivity with and without electrostatic interactions (Figure S1). The COF structures in the Crystallographic Information File (CIF) format extracted from the dataset are converted into orthogonal unit cells by AtomsK [7]. We calculate the thermal conductivity in two orthogonal in-plane directions (denoted as x and y) of COFs. To calculate κ_x (e.g., zigzag direction of honeycomb COFs), we repeat each orthogonal unit cell to a supercell of 7 nm by 2 nm in x and y directions, respectively (Figure S2i). Another supercell of 2 nm by 7 nm is created to calculate κ_y (e.g., armchair direction of honeycomb COFs). Each supercell contains one layer of 2D COF in the z (cross-plane) direction. Unit cell repetition and atom type assignment are done by the LAMMPS Interface package [8]. The initial configuration is minimized using the conjugate gradient method and equilibrated by consecutive runs under NPT and NVT ensembles. More specifically, the minimized structure is heated to 300 K in 60 K steps. Each heating step takes 100 ps under NVT followed by a 100-ps holding under NPT to relax the structure at constant temperature. The total equilibration time is 1 ns. During equilibration, the crystal structures of some COFs become unstable, leading to significant changes (mostly contraction) in the dimensions of the supercells. We filter 2,471 intact COFs after equilibration by selecting those whose relative change in supercell dimension is under 10%.

We employ the Non-Equilibrium Molecular Dynamics (NEMD) method to calculate in-plane thermal conductivities of COFs. In this setup, the equilibrated structure is divided into 100 bins with equal width in the direction of heat flow. The leftmost and rightmost bins are defined as cold sinks while the two bins in the middle are defined as heat sources (Figure S2i). Periodic boundary conditions are applied in all three directions. Equal amount of heat is added to each hot bin and subtracted from each cold bin by the enhanced heat exchange algorithm [9] at a rate proportional to the total number of atoms in the system:

$$\frac{dE}{dt} = k \cdot n_{\text{atom}}, \quad (1)$$

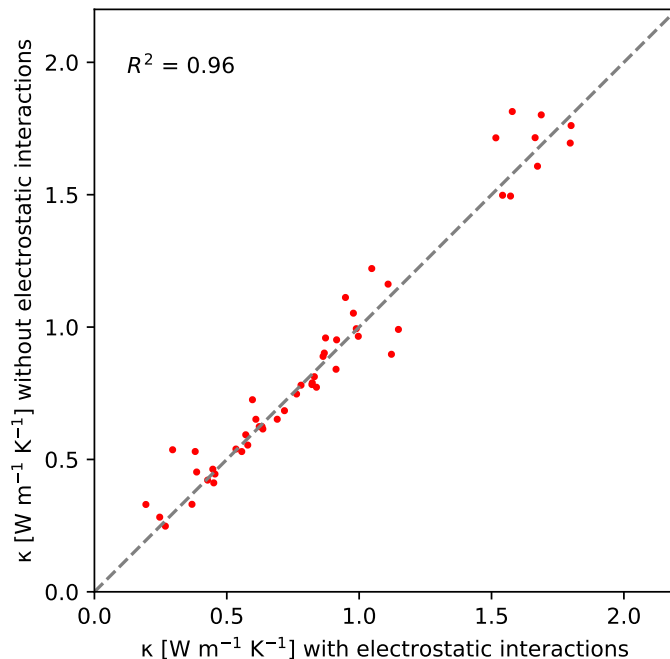


Figure S1: Comparison of thermal conductivity of 50 COFs by MD simulations without electrostatic interactions vs. with electrostatic interactions.

where the constant $k = 10^{-7} \text{ kcal} \cdot \text{mol}^{-1} \cdot \text{fs}^{-1}$. Since thermal conductivity is typically correlated with density, Equation 1 ensures a reasonable temperature difference between heat sources and cold sinks. This setup is maintained in NVE ensemble for 2 ns and the temperature of each bin except heat sources and cold sinks is recorded and averaged over the last 1 ns. Two temperature gradients are obtained from two halves of the system and fit to linear regressions (Figure S2j-m). The thermal conductivity is calculated by Fourier's law:

$$\kappa = \frac{1}{S} \frac{dE}{dt} \frac{dL}{dT}, \quad (2)$$

where S is the cross-sectional area perpendicular to the direction of heat flow and dT/dL is the average absolute slopes of the linear fits from both halves. The same method is used to calculate κ_x and κ_y on a total number of 2,471 COFs.

To validate our MD calculations, we calculated in-plane thermal conductivity κ of two 2D COFs with available experimental measurements in literature [10, 11] (COF-5 and TP-COF; structures presented in Figure S2d-e) and compared the results in Table S1. For each COF, three replicate simulations with different initial atomic velocities were performed and the mean and standard deviation of κ are reported. Our calculations agree reasonably well with experimental results, and the quantitative differences can be attributed to the inherent limitations, such as (i) we measure the in-plane thermal conductivity, while the reported values are for the cross-plane properties, and (ii) real COFs contain defects, such as vacancies, dislocations and grain boundaries [12, 13]. Our simulations consider perfect, defect-free structures and thereby exhibit different κ from the experimental measurements.

COF	In-plane κ by MD (W/mK)	Cross-plane κ by experiments [10, 11] (W/mK)
COF-5	1.48 ± 0.04	1.03
TP-COF	1.06 ± 0.02	0.89

Table S1: In-plane thermal conductivity κ of COF-5 and TP-COF calculated by MD simulations in this work and their cross-plane thermal conductivity measured by experiments in literature [10, 11].

To examine the effect of supercell dimension on calculated thermal conductivity, we calculate the average in-plane thermal conductivity (denoted as κ) of 5 COFs with thermal conductivity covering the entire range of the dataset and two existing COFs (COF-5 and TP-COF) (Figure S2b-h) with different supercell dimensions in heat transfer direction, as shown in Figure S2a. κ of all 7 COFs converges as the supercell dimension approaches 7 nm, confirming that the chosen dimension is sufficient to minimize the size effect.

The density of each COF is obtained from the equilibrated structure in MD simulations. The structural properties including the largest pore diameter (LPD), void fraction, and gravimetric surface area (GSA) are obtained directly from the dataset by Mercado et al. [1]

1.2 Minimal anisotropy in in-plane thermal conductivity

The distribution in Figure S3a shows that the majority of the κ_x/κ_y values cluster around 1.0, indicating that κ_x and κ_y are generally similar. This is further supported by the parity plot in Figure S3b, which exhibits a strong linear correlation ($R^2 = 0.968$) between κ_x and κ_y . These observations suggest that for most cases, the in-plane thermal conductivities are nearly equal. Therefore, we utilize average thermal conductivity κ as the quantity of interest to explore the structure-property relationships.

1.3 Feature distribution

Figure S4 illustrates the distribution of all features and their intercorrelations. Most features exhibit moderate to strong correlations, including: **(i)** an inverse correlation between void fraction and density, **(ii)** an inverse correlation between pore size and density, **(iii)** a strong positive correlation between void fraction and surface area, and **(iv)** a positive correlation between pore size and void fraction (and, by extension, with surface area). Notably, the dangling mass ratio (DMR) shows minimal correlation with other features, apart from **(v)** a moderate inverse correlation with surface area and a weaker inverse correlation with void fraction.

2 Ensemble Regression Models

Regression Model	R^2
Random Forest	0.592 ± 0.039
Gradient Boosting	0.536 ± 0.038
XGBoost	0.551 ± 0.060
AdaBoost	0.312 ± 0.103

Table S2: Performances of standard ensemble regression models at predicting κ using the four standard descriptors (excluding DMR): density, pore size, surface area, and void fraction. The table reports R^2 scores obtained through 10-fold cross-validation.

Regression performance excluding DMR as a feature: We trained four standard ensemble regression models— Random Forest [14], Gradient Boosting [15], XGBoost [16], and AdaBoost [17] —to predict the thermal conductivities of 2D Covalent Organic Frameworks (COFs) based on four features: Density, Pore Size, Void fraction, and Surface Area. The predictive performances of all models are outlined in Table S2.

Implementation Details: All models, including those incorporating DMR as a feature, were implemented using the scikit-learn library [18], except for the XGBoost regressor, which was sourced from the xgboost package [16]. Each model was configured with 100 estimators and trained on a 90/10% train-test split. To ensure robust evaluation, we performed 10-fold cross-validation to calculate confidence intervals for predictive performance.

3 Machine learning details

We split our dataset randomly into 80% for training, 10% for validation and the remaining data for testing. We fine-tune the (pre-trained) PMTransformer and jointly train a prediction head for 100 epochs. Throughout this fine-tuning phase, the model's performance was assessed at each epoch using the validation subset. This evaluation serves as a checkpoint mechanism to save the model parameters only when there was an observable improvement in the predictive performance on the validation data. This step is necessary in preventing overfitting and ensuring that the model generalizes well to unseen data. Upon completion of the fine-tuning phase, the optimized model was subjected to a final evaluation using the test subset, which had not been exposed to the model during training. The prediction accuracies are reported on the test set. We use a batch size of 32, and fine-tune the model using the AdamW [19] optimizer at a learning rate of 0.0001, and a default weight decay of 0.01.

4 Dangling mass computation

Dangling atoms are defined in contrast to the main branch in COF structures. Specifically, within a unit cell, atoms located on the boundary are termed boundary atoms (represented by black atoms in S5). The shortest paths that connect all boundary atoms are identified as the main branch (yellow atoms in S5). Note that boundary atoms are also labelled as part of the main branch. Atoms that are not part of the main branch are considered dangling branches (red atoms in S5). Notably, if a ring contains more than three atoms on the main branch, the ring is considered rigid, and the remaining atoms within the ring are not classified as dangling atoms. The total mass of the dangling atoms in a unit cell is referred to as the dangling mass. To distinguish, dangling hydrogen atoms are shown in lighter red, while the remaining heavier dangling atoms are shown in red.

5 More examples of COFs and the effect of dangling mass

In Figure S6 we present additional examples of the influence of dangling mass in COFs. In Figure S7 we illustrate the phonon spectral energy density (pSED) maps for all example COFs and their dangling counterparts, which were introduced in Figure 4 of the main article and the additional examples in Figure S6. For the visualization of the pSED profiles of each COF pair, the lower bound of the colorbar is defined as the minimum value across both logarithmic pSED profiles, while the upper bound is set as the maximum value across both logarithmic pSED profiles up to 99 percentile to enhance contrast. These bounds are maintained consistently across each pair to ensure a meaningful comparison. The distribution of logarithmic pSED values for an example COF is presented in Figure Figure S8.

6 Vibrational density of states and phonon spectral energy density calculation

To calculate vibration density of states (VDOS) of atoms, each equilibrated COF structure is first relaxed under NVE ensemble for 1 ns followed by a 0.1-ns NVE production period, where atomic velocities are recorded every 5 fs. VDOS is calculated by the Fourier transform of the normalized velocity autocorrelation function (VACF) of a specific group of atoms β :

$$\text{VDOS}^\beta(\omega) = \mathcal{F}(\text{VACF}^\beta(t)) \quad (3)$$

and

$$\text{VACF}^\beta(t) = \frac{\sum_{i \in \{x,y,z\}} \sum_{j \in \beta} \langle v_i^j(t_0 + t) v_i^j(t_0) \rangle}{\sum_{i \in \{x,y,z\}} \sum_{j \in \beta} \langle v_i^j(t_0) v_i^j(t_0) \rangle}, \quad (4)$$

where β is the interested group of atoms, \mathcal{F} is the Fourier transform, ω is frequency, v_i^j is the velocity of atom j in i direction, t is correlation time and $\langle \rangle$ is the average over all time origins t_0 .

The phonon spectral energy density (pSED) of COFs is calculated from MD simulations using the following equation [20]:

$$\Phi(\mathbf{q}, \omega) = \frac{1}{4\pi\tau_0 N_T} \sum_{\alpha \in \{x,y,z\}} \sum_{b=1}^B m_b \left| \int_0^{\tau_0} \sum_{n=1}^{N_T} \dot{u}_\alpha(n, b; t) \times \exp(i\mathbf{q} \cdot \mathbf{r}(n, 0; t) - i\omega t) dt \right|^2, \quad (5)$$

where \mathbf{q} is the wave vector, ω is the frequency, τ_0 is the simulation time, N_T is the number of unit cells in the simulation supercell, α is the direction, b is the label of each atom in the unit cell, B is the number of atoms in the unit cell, m_b is the mass of atom b , n is the label of each unit cell in the simulation supercell, $\dot{u}_\alpha(n, b; t)$ is velocity in the direction α at time t of atom b in unit cell n , and $\mathbf{r}(n, 0; t)$ is the equilibrium position of unit cell n . The positions and velocities of each atom are extracted from MD simulations under the NVE ensemble.

7 Computing time and resource estimates

Table S3 lists the runtime and resources used for different tasks. The computing times are meant to provide only a qualitative impression, as different software architectures and hardware environments were used for each task.

Task	Software	Parallelization & Hardware	Runtime [‡]
Computing κ in one in-plane direction	LAMMPS [2]	CPU, no parallelization [¶]	150 hours [†]
Predicting κ with PMTransformer	PMTransformer in Python	1x NVIDIA A5000 GPU	0.07 seconds [†]
Energy grid computation	GRIDAY [21]	CPU, no parallelization	3 seconds [†]
Fine-tuning the PMTransformer	PMTransformer in Python	3x NVIDIA A5000 GPUs	1 hour
VDOS computation	LAMMPS	8 MPI Cores	12 hours [†]
Training regression models with 10-fold CV	Scikit-learn in Python	CPU, no parallelization	20 seconds

Table S3: Runtime, software, parallelization, and hardware resources used for different tasks. [‡]Runtimes reported are rough estimates only and may vary across different simulations and hardware. [†]Runtimes reported for predictions via PMTransformer and MD computations are averages for one sample. [¶]Tasks are performed on the Oracle Cloud Infrastructure (OCI).

References

- [1] R. Mercado, R.-S. Fu, A. V. Yakutovich, L. Talirz, M. Haranczyk, B. Smit, *Chemistry of Materials* **2018**, *30*, 15 5069–5086.
- [2] A. P. Thompson, H. M. Aktulga, R. Berger, D. S. Bolintineanu, W. M. Brown, P. S. Crozier, P. J. in 't Veld, A. Kohlmeyer, S. G. Moore, T. D. Nguyen, R. Shan, M. J. Stevens, J. Tranchida, C. Trott, S. J. Plimpton, *Computer Physics Communications* **2022**, *271* 108171.
- [3] S. L. Mayo, B. D. Olafson, W. A. Goddard, *Journal of Physical chemistry* **1990**, *94*, 26 8897.
- [4] A. Giri, A. M. Evans, M. A. Rahman, A. J. McGaughey, P. E. Hopkins, *ACS nano* **2022**, *16*, 2 2843.
- [5] S. Thakur, A. Giri, *Journal of Materials Chemistry A* **2023**, *11*, 35 18660.
- [6] A. Yu, W. Liu, W. Xi, M. Mu, L. Shi, *Chemistry of Materials* **2024**, *36*, 4 1880.

- [7] P. Hirel, *Computer Physics Communications* **2015**, *197* 212–219.
- [8] P. G. Boyd, S. M. Moosavi, M. Witman, B. Smit, *The Journal of Physical Chemistry Letters* **2017**, *8*, 2 357–363.
- [9] P. Wirsberger, D. Frenkel, C. Dellago, *The Journal of Chemical Physics* **2015**, *143*, 12.
- [10] J. Kwon, H. Ma, A. Giri, P. E. Hopkins, N. B. Shustova, Z. Tian, *ACS Nano* **2023**, *17*, 16 15222–15230.
- [11] A. M. Evans, A. Giri, V. K. Sangwan, S. Xun, M. Bartnof, C. G. Torres-Castanedo, H. B. Balch, M. S. Rahn, N. P. Bradshaw, E. Vitaku, D. W. Burke, H. Li, M. J. Bedzyk, F. Wang, J.-L. Brédas, J. A. Malen, A. J. H. McGaughey, M. C. Hersam, W. R. Dichtel, P. E. Hopkins, *Nature Materials* **2021**, *20*, 8 1142–1148.
- [12] S. Daliran, M. Blanco, A. Dhakshinamoorthy, A. R. Oveisi, J. Alemán, H. García, *Advanced Functional Materials* **2024**, *34*, 18 2312912.
- [13] S. Daliran, A. R. Oveisi, A. Dhakshinamoorthy, H. Garcia, *ACS Applied Materials & Interfaces* **2024**, *16*, 38 50096.
- [14] L. Breiman, *Machine Learning* **2001**, *45*, 1 5–32.
- [15] J. H. Friedman, *The Annals of Statistics* **2001**, *29*, 5.
- [16] T. Chen, C. Guestrin, In *Proceedings of the 22nd ACM SIGKDD International Conference on Knowledge Discovery and Data Mining*, volume 11 of *KDD '16*. ACM, **2016** 785–794, URL <http://dx.doi.org/10.1145/2939672.2939785>.
- [17] Y. Freund, R. E. Schapire, *Journal of Computer and System Sciences* **1997**, *55*, 1 119–139.
- [18] F. Pedregosa, G. Varoquaux, A. Gramfort, V. Michel, B. Thirion, O. Grisel, M. Blondel, P. Prettenhofer, R. Weiss, V. Dubourg, J. Vanderplas, A. Passos, D. Cournapeau, M. Brucher, M. Perrot, E. Duchesnay, *Journal of Machine Learning Research* **2011**, *12* 2825.
- [19] I. Loshchilov, F. Hutter, Decoupled weight decay regularization, **2017**, URL <https://arxiv.org/abs/1711.05101>.
- [20] J. A. Thomas, J. E. Turney, R. M. Iutzi, C. H. Amon, A. J. McGaughey, *Physical Review B—Condensed Matter and Materials Physics* **2010**, *81*, 8 081411.
- [21] GitHub - Sangwon91/GRIDAY: Energy shape calculator for the porous materials — github.com, <https://github.com/Sangwon91/GRIDAY>, [Accessed 14-06-2024].

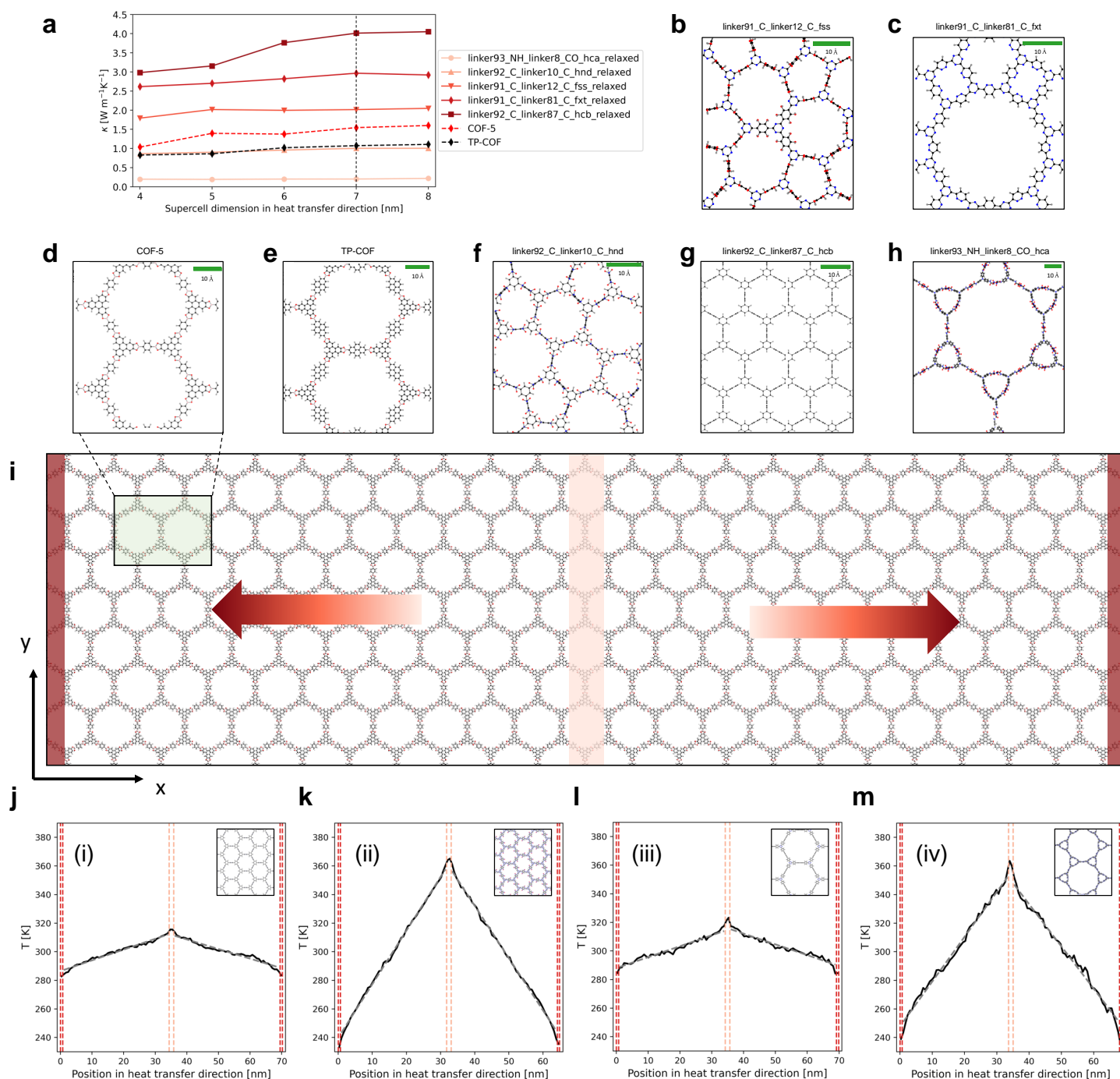


Figure S2: Schematic of calculation of in-plane thermal conductivities of COFs by NEMD simulations. **(a)** Average thermal conductivity κ as a function of supercell dimension in heat transfer direction. **(b-h)** Orthogonal unit cells of the COFs used in the convergence study. **(i)** COF-5 supercell created by repeating the unit cell in x and y directions. The supercell is divided into 100 bins. The middle two bins are set as heat sources while the two bins nearest to the boundary are set as cold sinks. **(j-m)** The average temperature of each bin for each example COF in Figure 2 of the main article. The spatial temperature distribution is fitted using linear regressions (grey dashed lines) to obtain temperature gradients.

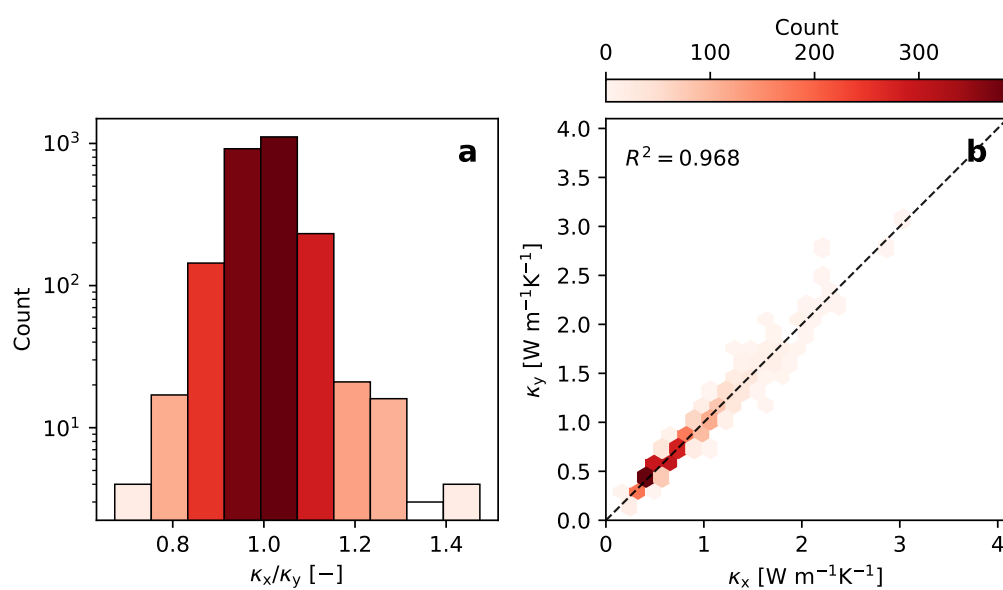


Figure S3: (a) Distribution of the ratio of in-plane thermal conductivities (κ_x/κ_y), (b) parity plot comparing κ_x and κ_y .

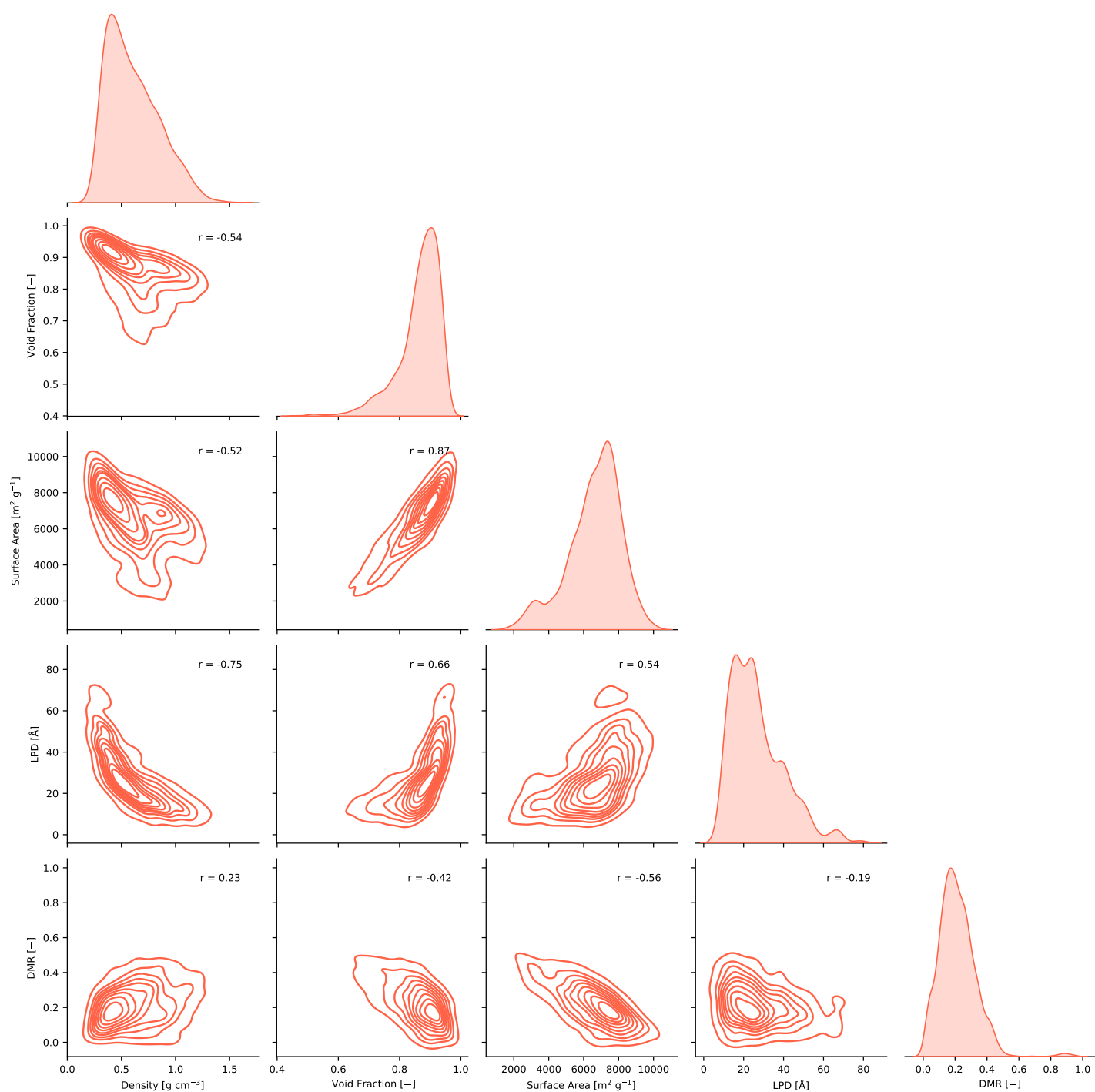


Figure S4: Distribution and pairwise correlations of the five features: density, void fraction, surface area, pore size, and dangling mass ratio. Pearson correlation coefficients are shown in each joint distribution plot.

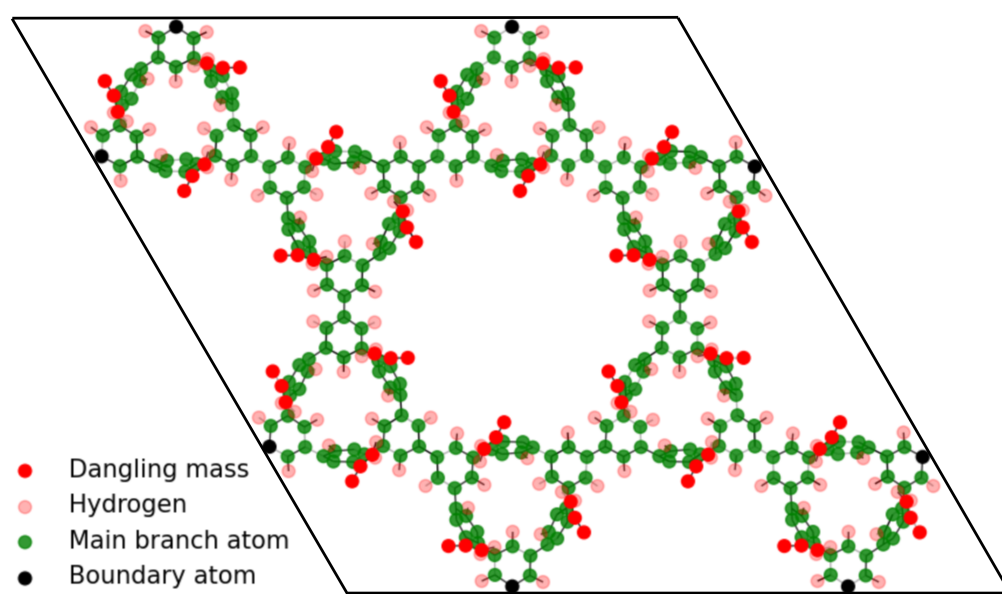


Figure S5: A COF unit cell with atoms either labeled as part of the main branch or as dangling atoms.

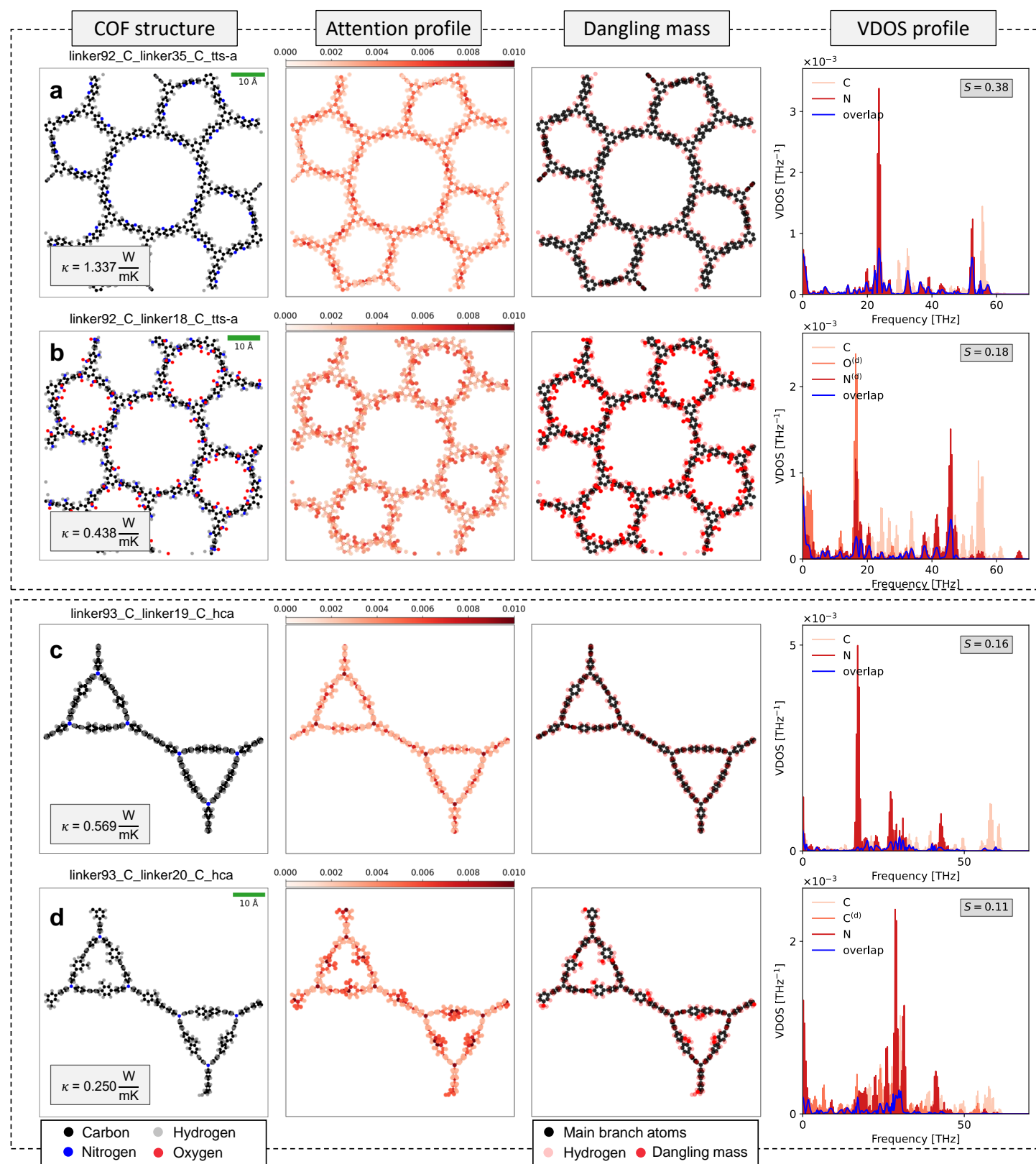


Figure S6: Two example pairs (contained in dashed boxes) of COFs with same topologies, similar geometric descriptors, but contrasting thermal conductivities. The first column illustrates the COF structures. The second column shows the atom-level attention score profile computed by the attention mechanism. The third column shows the same COF structure distinguishing atoms on the main branch and dangling atoms (with separate distinction for hydrogen atoms). The fourth column shows the VDOS profiles of various groups of atoms within the corresponding COF structure with the overlap metric S . The legend indicates the VDOS profile for main branch atoms (.) and dangling atoms (.)^(d).

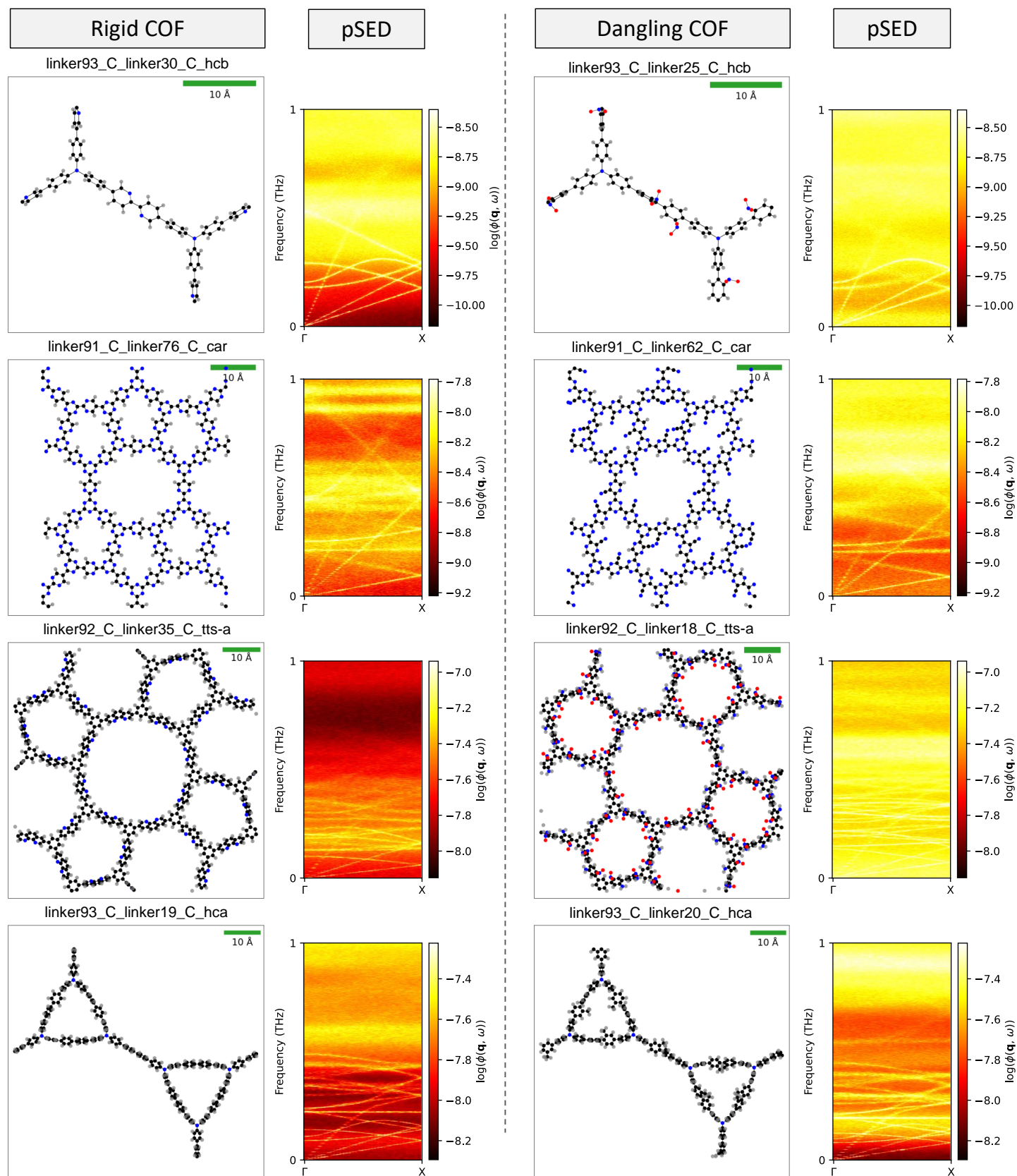


Figure S7: Phonon spectral energy density (pSED) maps of all example COFs and their dangling counterparts. For each pair of COFs, the lower bound of the colorbar is set as the minimum value across both pSED profiles. The upper bound is set as the maximum value across both pSED profiles up to 99 percentile to add contrast.

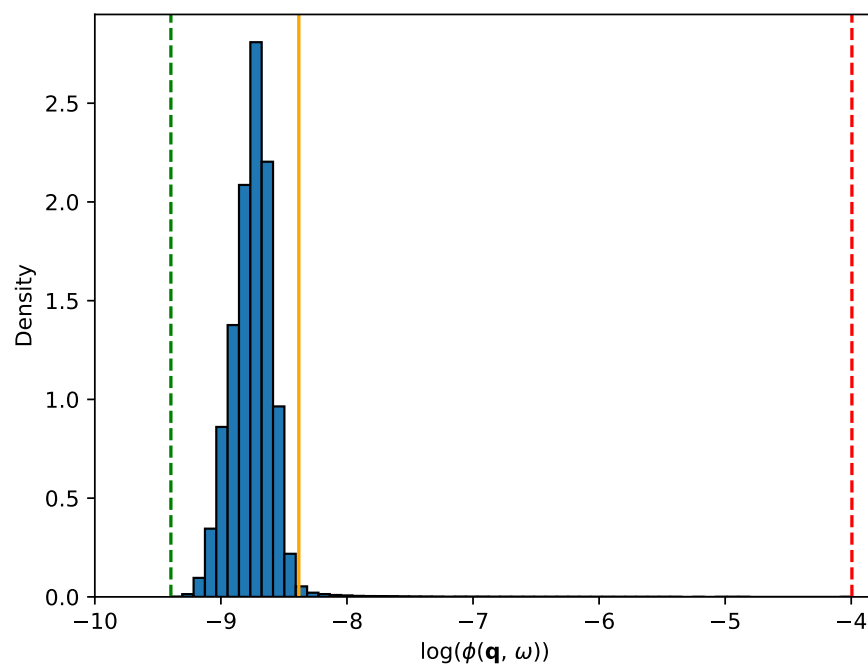


Figure S8: Distribution of logarithm pSED values for an example COF (linker93_C_linker25_C_hcb, structure presented in Figure S7).